DOI: 10.21062/mft.2025.064 http://www.journalmt.com

Hydrogen Embrittlement of Ferritic-Perlitic and Martenzitic Pipe Steels

Anna Knaislová (0000-0002-3508-9725), Jan Zmeko, Matěj Reiser, Nikola Macháčková (0000-0003-0903-2909), Dalibor Vojtěch (0000-0002-6910-3206)
Department of Metals and Corrosion Engineering, University of Chemistry and Technology, Prague. Technická 5, 166 28 Prague, Czech Republic

This study investigates the susceptibility of two pipeline steels, ferritic–pearlitic CSN 12022 and martensitic L80, to hydrogen embrittlement. Electrolytic hydrogen charging increased the absorbed hydrogen content approximately fivefold in both steels, with the martensitic grade showing higher uptake due to its dense dislocation network and carbide distribution. Tensile tests demonstrated that hydrogen had little influence on yield or ultimate tensile strength but caused a severe reduction in ductility. Elongation dropped from 39 % to 13 % in CSN 12022 and from 25 % to 11 % in L80. Fractographic analysis confirmed a transition from ductile dimple fracture to quasi-cleavage fracture in the hydrogen-charged condition. These findings confirm that microstructure strongly affects hydrogen embrittlement: ferritic–pearlitic steel undergoes a more dramatic relative loss in ductility, while martensitic steel retains higher strength but exhibits significant hydrogen-assisted cracking. The results highlight the importance of considering hydrogen effects in the design and application of steels for energy and gas transport systems.

Keywords: Hydrogen embrittlement, Mechanical properties, Tensile tests, CSN 12022 steel, L80 steel

1 Introduction

The CSN 12022 ferritic-pearlitic steel (Tab. 1) belongs to the group of non-alloy structural carbon steels with a carbon content in the range of 0.15–0.22%. It also contains silicon and manganese, which improve strength and toughness, while the phosphorus and sulfur contents are limited to preserve good ductility [1, 2]. Trace amounts of chromium, nickel, and copper occur mainly as a result of production processes and have no significant effect on the basic properties. This steel exhibits a balanced combination of mechanical properties, making it suitable for a wide range of structural applications. It offers good strength, toughness, and plasticity, as well as good machinability and weldability, which further expand its range of uses [3, 4]. In practice, CSN 12022 is employed in engineering and construction for the manufacture of components subjected to static and dynamic loads—such as shafts, pins, fasteners, support frames, and other machine parts. It is also suitable for pipes, tanks, and structural units that require a combination of strength, toughness, and good processability [5]. A specific issue for this steel is hydrogen embrittlement, which manifests as a reduction in toughness and ductility caused by the diffusion of atomic hydrogen into the metal lattice [[6, 7]. Thanks to its combination of good processability, balanced mechanical properties, and relative toughness even at lower temperatures, CSN 12022 is a versatile structural steel. When used in environments containing hydrogen (for example, in the chemical industry, or in hydrogen storage or transport), the risk of hydrogen embrittlement must be considered, and both design and operating conditions should be adapted accordingly [8].

Tab. 1 *Composition of the CSN 12 022 steel*

Element	C	Mn	Si	Cr	Ni	Cu	P	S
Composition [%]	0.15 – 0.22	0.5 – 0.8	0.17-0.37	max 0.25	max 0.25	max 0.25	max 0.04	max 0.04

The L80 steel is a martensitic low-alloy steel (Tab. 2) primarily used in the oil and gas industry, especially for seamless pipes in compliance with the API 5CT standard [6, 7]. Its chemical composition features a medium carbon content (typically 0.2–0.3%) and alloying with manganese, silicon, and smaller amounts of chromium and molybdenum [9]. These elements increase strength, hardenability, and wear resistance, while the sulfur and phosphorus contents are strictly limited to maintain toughness and good workability [10]. The martensitic structure is obtained through heat treatment (quenching and tempering), providing high tensile strength and good resistance to mechanical wear [11]. L80 steel also maintains sufficient toughness for use in high-pressure and high-load environments. Thanks to these properties, it is widely used for drilling and production tubing, casing strings, and components exposed to demanding mechanical and corrosive conditions [7]. A significant issue for this steel is hydrogen embrittlement. The ingress of atomic

hydrogen into the crystal lattice reduces the ductility and toughness of the material [12-14]. L80 steel combines high strength, wear resistance, and sufficient toughness, making it suitable for demanding applications in the extraction industry. When used in hydrogen-containing environments, the risk of hydrogen embrittlement must be considered, and appropriate measures should be taken in design and operation [15].

Tab. 2 *Composition of the L80 steel*

Element	C	Mn	Si	Cr	Ni	Cu	P	S
Composition [%]	max 0.43	max 1.9	max 0.45	-	max 0.25	max 0.35	max 0.03	max 0.03

The purpose of this study is to compare the effect of hydrogen embrittlement on the mechanical properties of two steels, CSN 12022 and L80, which differ in their manufacturing processes and microstructures. The experimental results obtained from tensile tests and fractographic analysis will be used to assess their resistance to this phenomenon and to propose recommendations for their practical application.

2 Experimental

The microstructure was observed on a Nikon Eclipse MA 200 metallographic light-optical microscope. Hydrogen charging of the test specimens was performed by electrolysis. A small plexiglass container was attached around the gauge section of each specimen and filled with electrolyte (Fig. 1). The hydrogen charging process took place directly on the tensile testing machine with hydraulic grips. Charging was conducted for 30 minutes prior to the tensile test and continued throughout the test until specimen failure. The electrolyte used was a solution of 0.1 M H_2SO_4 with an addition of 2 g/l of cyanate. A two-electrode setup was used, with a platinum electrode and a DC laboratory power supply. During the entire test, the electric current was maintained at 0.1 A. One side of the test specimen was coated with a speckle pattern for deformation tracking using the DIC system. The resulting current density was approximately 25 mA/cm². A detailed view of the clamped test specimen with the electrolyte and container just before the start of the tensile test is shown in Fig. 1. The hydrogen content was measured using a Bruker G8 Galileo elemental fusion analyzer.

Mechanical property testing was carried out in the form of tensile tests. A static tensile test of the initial state was carried out at room temperature, as well as a static test under hydrogen charging conditions at room temperature. Ready-made flat test specimens made from two types of steel were provided. The geometry of the test specimens is shown in Fig. 2. For simplicity, the test specimens were labeled as 12 and L80. In both cases, the material was taken directly from piping shown in Fig. 3.

Tensile tests on hydrogen-charged samples were carried out using the same testing machine as for the initial state. Deformation was measured using the Aramis DIC system (see Fig. 1). The crosshead displacement rate was again set to 0.45 mm/min. A total of three tests were conducted for each type of steel.

The appearance of the fracture surfaces of the samples after uniaxial tensile testing was documented using a Tescan Vega 3 scanning electron microscope.

The tensile tests were performed using a Mayes servo-electric testing machine with a load capacity of 100 kN (see Fig. 4). A mechanical MTS extensometer was used to measure deformation. The crosshead displacement rate was set to 0.45 mm/min. A total of three tests were carried out for each type of steel.

Fig. 1 *Close-up of the container with electrolyte and the clamped test specimen*

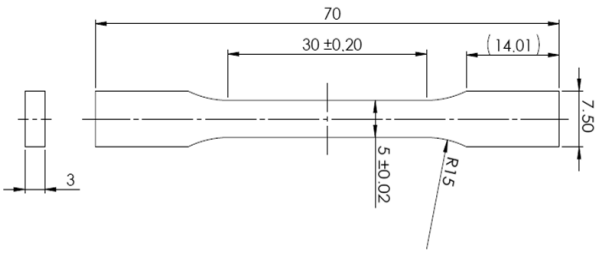

Fig. 2 *Geometry of flat test specimens for tensile testing*

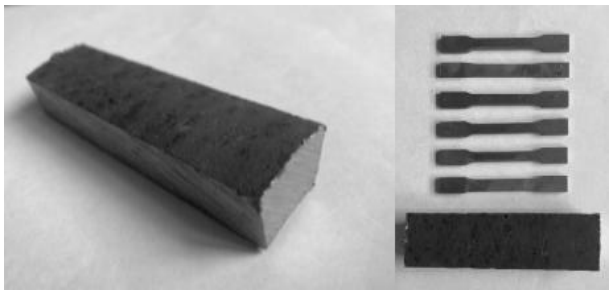

Fig. 3 *The supplied material and test specimens*

ISSN 1213–2489
e-ISSN 2787–9402

Fig. 4 *Mayes testing machine with a load capacity of 100 kN*

3 Results

3.1 Microstructure and hydrogen content in steel samples

First, the microstructure on metallographic light-optical microscope was observed. The microstructure of steel CSN 12022 (Fig. 5a) consists of polyhedral ferrite phase (light-appearing grains) and pearlite microstructural constituent (darkappearing grains) consisting of the alternating ferrite and cementite lamellae structures, which is predominantly located along the ferrite grain boundaries and, in some cases, forms colonies within the grains [16, 17]. The structure corresponds to the condition after normalizing annealing and exhibits a relatively coarse-grained ferritic–pearlitic character with a non-uniform distribution of pearlite. This type of microstructure provides good ductility and toughness at medium strength levels. The microstructure of martensitic steel L80 (Fig. 5b) consists of fine-grained tempered martensite with a uniform distribution of fine carbides. The structure results from quenching from the austenitizing temperature followed by tempering, which relieves internal stresses and improves toughness while maintaining high strength.

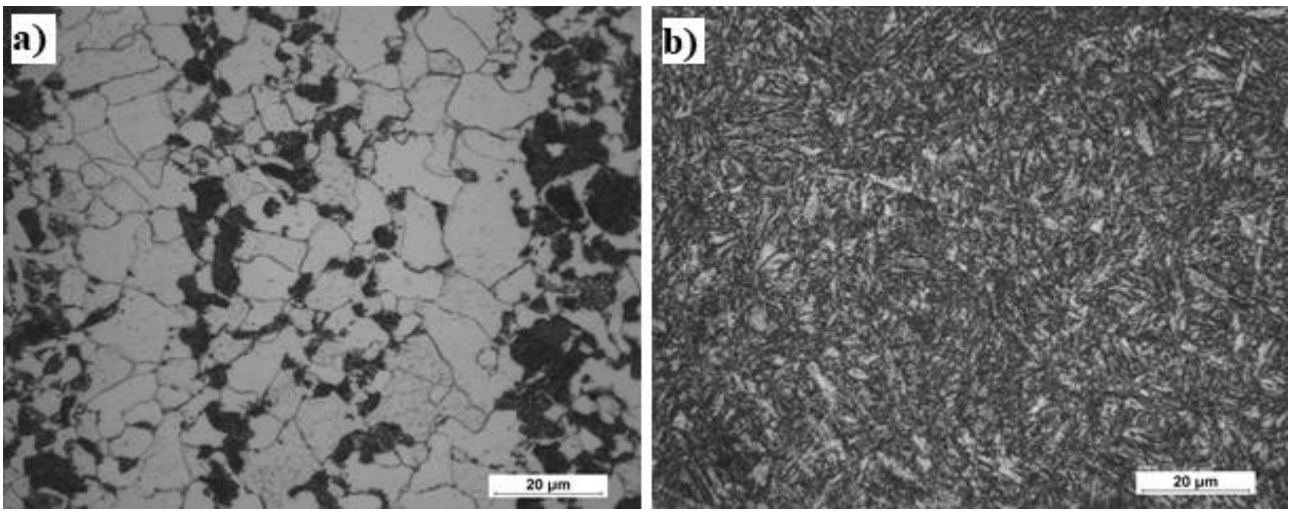

Fig. 5 *Microstructure: a) 12022, b) L80*

The results of the hydrogen analysis in the samples are presented in Table 3. In the as-received condition, steel CSN 12 022 exhibited an average hydrogen content of 3.07 ppm with a relatively low scatter, while martensitic steel L80 showed a somewhat higher average value of 5.04 ppm with greater variability. Electrolytic hydrogen charging led to a pronounced increase in hydrogen concentration in both materials. For CSN 12022, the hydrogen content rose to an average of 15.02 ppm, representing an approximately fivefold increase compared to the initial state. In contrast, steel L80 experienced an even more substantial effect, with the average hydrogen content increasing to 24.73 ppm—almost five times higher than its baseline value. The martensitic structure facilitates the ingress and retention of hydrogen more than the ferritic-pearlitic one because it contains a high density of defects (dislocations, carbides, stresses) that act as hydrogen traps. Therefore, martensitic steels are more susceptible to hydrogen embrittlement than classic low-carbon ferritic-pearlitic steels. The scatter of the measured values after hydrogen charging was notably larger in both cases, indicating less uniform hydrogen uptake among specimens. This greater variability is likely related to differences in surface condition, local microstructural features, and the interaction between microstructure and hydrogen diffusion.

indexed on http://www.webofscience.com and http://www.scopus.com

Tab. 3 *Hydrogen content in steel samples, in ppm*

Material condition	CSN 12022 – Initial State	CSN 12022 – Hydrogen-Charged	L80 – Initial State	L80 – Hydrogen-Charged
Average	3.07	15.02	5.04	24.73
σ_{n-1}	0.37	4.66	4.10	12.9

3.2 Mechanical properties

The test specimens after the static tensile test of the initial state at room temperature are shown in Fig. 7. The measured values from the tensile tests are presented in Table 4. In the initial state, the ferrite–pearlite steel 12 022 exhibits lower yield and tensile strength (391 and 547 MPa, respectively) but significantly higher elongation (38.8 %) compared to the martensitic L80 grade (644 and 725 MPa, 25.0 %). After hydrogen charging (0.1 A, 0.5 h), both steels show pronounced embrittlement, manifested mainly as a loss of ductility. In 12 022, elongation decreases drastically from 38.8 % to 13.0 %, while strength remains nearly unchanged, though scatter in yield strength increases considerably. In contrast, L80 maintains similar strength levels (680 and 716 MPa) but its elongation drops from 25.0 % to 10.8 %. The ferrite–pearlite steel demonstrates a more severe relative reduction in ductility and less uniform behaviour after hydrogen absorption, whereas the martensitic steel retains higher strength but remains susceptible to hydrogen-induced embrittlement, ending with very limited ductility. Hydrogen clearly reduces the ability of both steels to plastically deform, with a much more pronounced embrittling effect on ductility than on strength. This behavior is typical for hydrogen embrittlement in steels: hydrogen either weakens interatomic bonds (Hydrogen-Enhanced Decohesion) or facilitates dislocation motion and localized slip (Hydrogen-Enhanced Localized Plasticity), both mechanisms leading to early fracture. The results highlight that martensitic microstructures, despite their higher strength, are not immune to hydrogen-induced embrittlement and can even exhibit greater susceptibility compared to ferritic–pearlitic steels due to their higher density of trapping sites.

Tab. 4 *Results of tensile tests of of the initial state at room temperature and hydrogen-charged samples*

	12022			L80			12022 H2_0,1A0,5h			L80 H2_0,1A0,5h		
	$YS_{0,2}$ [MPa]	UTS [MPa]	EL [%]	$YS_{0,2}$ [MPa]	UTS [MPa]	EL [%]	$YS_{0,2}$ [MPa]	UTS [MPa]	EL [%]	$YS_{0,2}$ [MPa]	UTS [MPa]	EL [%]
Average	391	547	38.8	644	725	25.0	438	547	13.0	680	716	10.8
σ_{n-1}	2.6	1.5	1.0	3.6	2.1	0.9	15.7	5.2	0.4	0.7	0.7	1.6

The tensile curves constructed from the data recorded by the testing machine are shown in Fig. 6. The tensile curves clearly demonstrate the embrittling effect of hydrogen on both steels. The stress–strain curve presented in Fig. 6 exhibits a pronounced upper and lower yield point (ReH and ReL), which is characteristic of ferritic–pearlitic steels. This behavior can be attributed to the presence of interstitial atoms, mainly carbon and nitrogen, in solid solution within the ferritic matrix. At the beginning of plastic deformation, mobile dislocations are temporarily pinned by these interstitial atoms, causing an accumulation of stress that leads to the distinct upper yield point. Once the stress is sufficient to unpin the dislocations, a sudden drop in flow stress occurs, followed by the formation and propagation of Lüders bands, which manifest as the yield plateau on the curve. The slight enhancement of this effect in the tested material may also be related to hydrogen interactions with dislocations, since hydrogen can further hinder their motion by forming local atmospheres around dislocation cores. After this transient stage, a stable plastic flow is established, governed by conventional dislocation glide. The observed yielding behavior therefore reflects the combined influence of interstitial solute pinning and hydrogen–dislocation interactions on the early stages of plastic deformation in ferritic–pearlitic steel. For the ferritic–pearlitic steel 12 022, hydrogen charging results in a significant reduction of elongation, with fracture occurring at much lower strain levels compared to the uncharged state. Interestingly, the yield strength of 12 022 is slightly increased after hydrogen exposure, while the ultimate tensile strength remains nearly unchanged, indicating that hydrogen primarily suppresses the ductility rather than the load-bearing capacity. In contrast, the martensitic steel L80 shows only a minor reduction in tensile strength upon hydrogen charging, but the ductility is severely reduced, with the material fracturing at around half of the elongation of the uncharged state. This pronounced loss of plasticity in both steels confirms the strong susceptibility of their microstructures to hydrogen-assisted cracking, although the mechanism differs: in ferritic–pearlitic steel it is mainly due to premature plastic instability, while in martensitic steel it is associated with hydrogen trapping and crack initiation along high-stress sites.

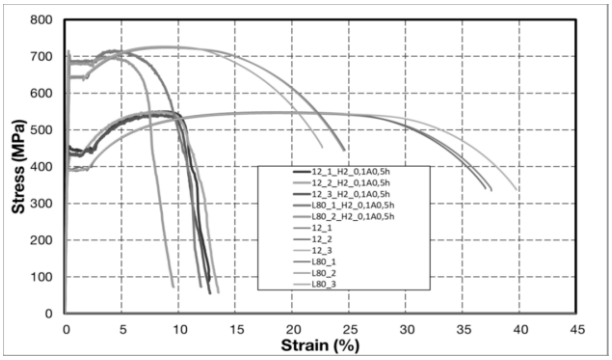

Fig. 6 *Comparison of tensile curves of hydrogen-charged and uncharged test specimens*

The test specimens after the static tensile test on samples without hydrogen and hydrogen-charged samples at room temperature are shown in Fig. 7 and 8. After each test, the specimen was immediately rinsed with clean water, dried with a hot air gun, and then preserved with WD-40 oil to prevent corrosion of the fracture surface and specimen surface. In the L80 specimens, a large number of cracks were observed in the necking area (see Fig. 9) suggesting a high brittleness of the hydrogen-charged martenzitic steel.

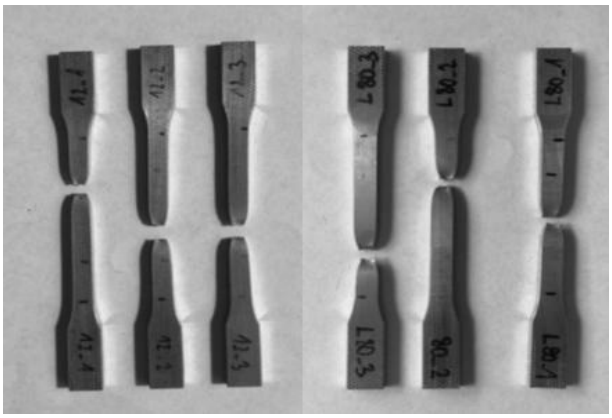

Fig. 7 *Test specimens after static tensile testing without hydrogen*

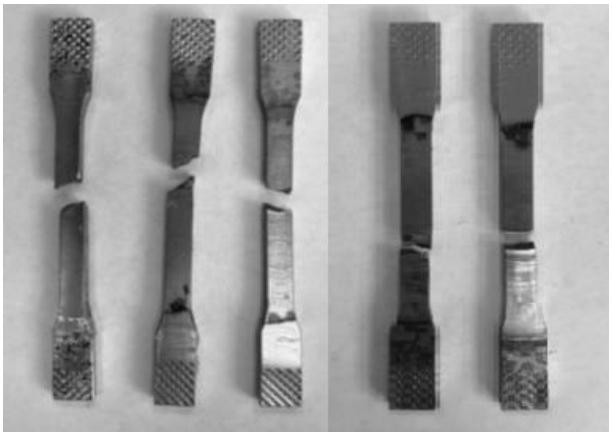

Fig. 8 *Test specimens after static tensile testing in an electrolytic hydrogen environment. On the left: CSN 12022; on the right: L80 specimens*

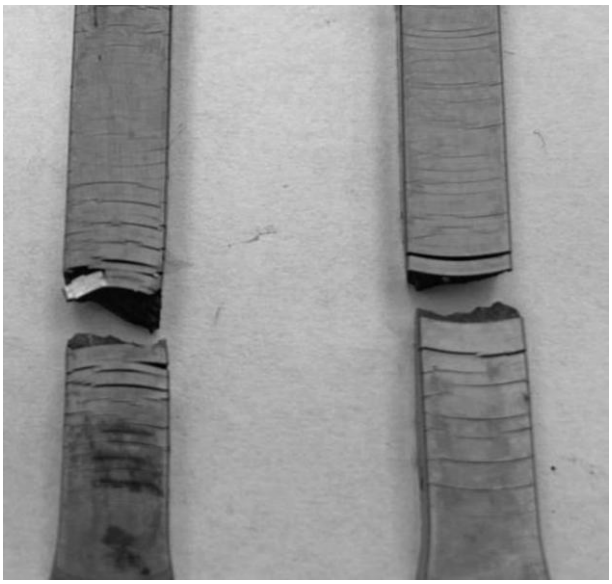

Fig. 9 *Close-up of the fracture area of the L80 test specimens*

4 Fracture surfaces of the samples after uniaxial tensile testing

Fracture surfaces of the "CSN 12022 initial state" samples at different magnifications are shown in Fig. 10. Fracture surfaces of the "L80 initial state" samples at different magnifications are shown in Fig. 11. The fracture surfaces of both steels in the initial states show practically no differences. In both cases, significant signs of plastic deformation are present on the fracture surfaces (irregular surface, dimpled morphology). No internal flaws were found on the fracture surfaces. Both steels exhibited noticeable necking at the fracture locations.

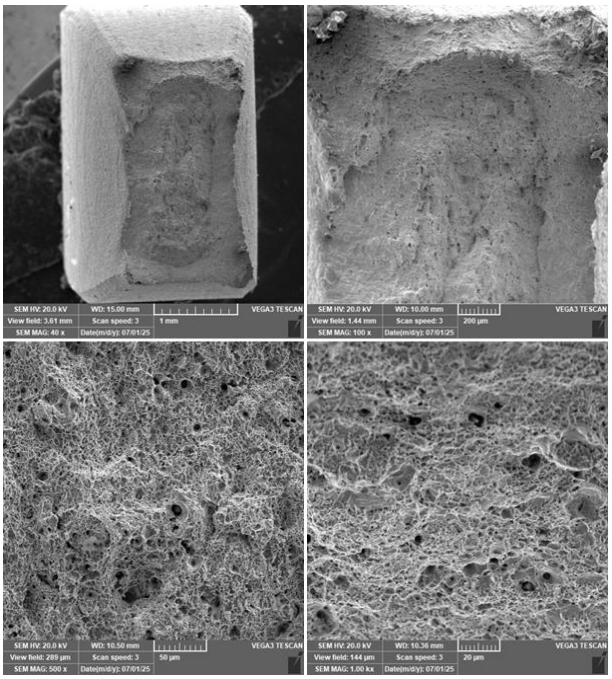

Fig. 10 *Fracture surface of the "CSN 12022 initial state" sample*

ISSN 1213–2489
e-ISSN 2787–9402

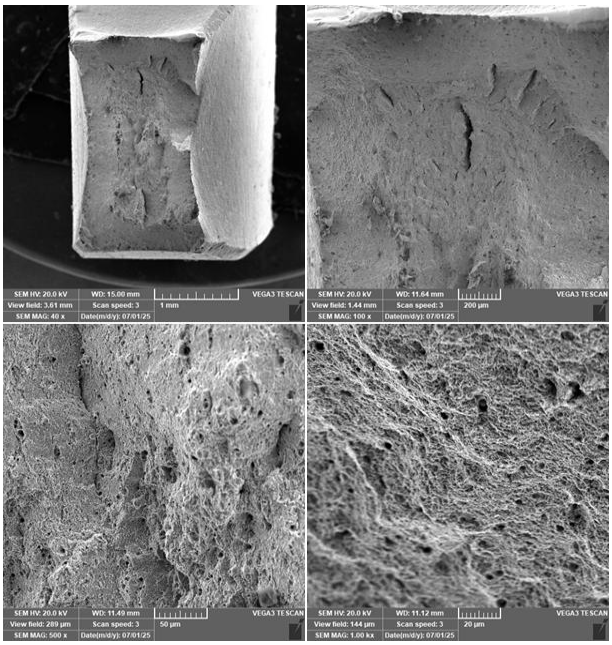

Fig. 11 *Fracture surface of the "L80 initial state" sample*

Fracture surfaces of the "ČSN 12 022 hydrogen-charged" samples at different magnifications are shown in Fig. 12. Fracture surfaces of the "L80 hydrogen-charged" samples at different magnifications are shown in Fig. 13. The fracture surfaces of both steels after hydrogen charging again show practically no differences between each other. In the hydrogen-charged samples, the fracture surfaces were significantly less irregular. No internal flaws were detected on these fracture surfaces either. The markedly more "brittle" nature of the fractures was also indicated by the significantly lower reduction in cross-sectional area at the fracture sites.

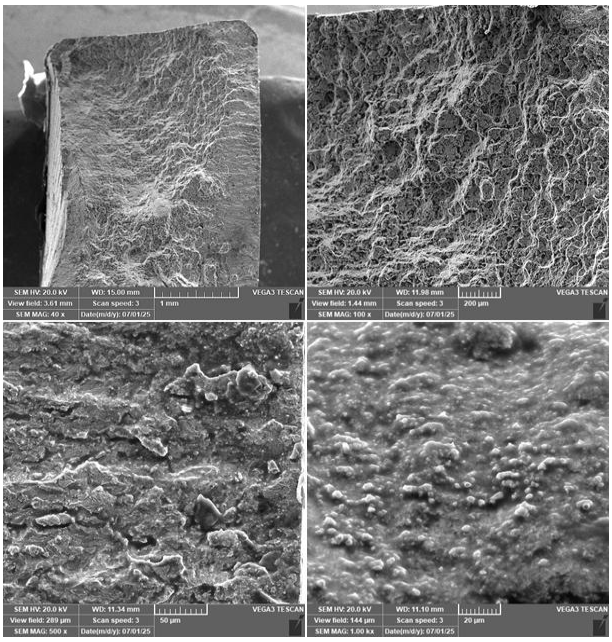

Fig. 12 *Fracture surface of the "CSN 12022 hydrogen-charged" sample*

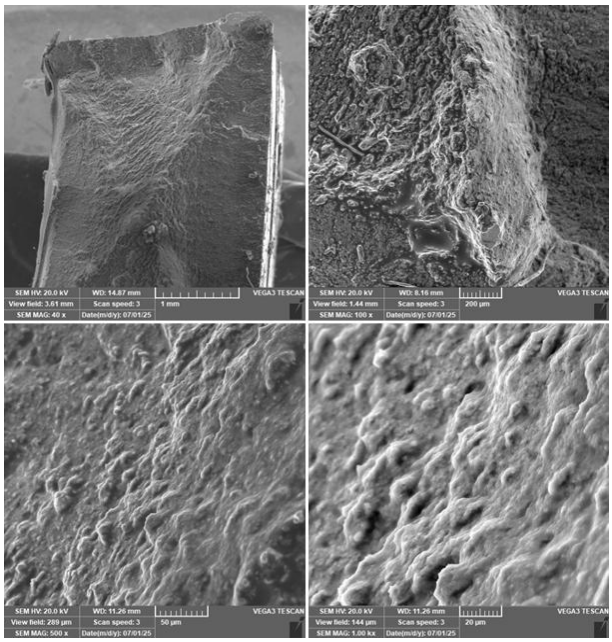

Fig. 13 *Fracture surface of the "L80 hydrogen-charged" sample*

5 Discussion

The experimental results clearly show that hydrogen causes only minor changes in yield and tensile strength but leads to a pronounced loss of ductility in both steels. In ferritic–pearlitic CSN 12022, elongation was reduced by nearly 70 %, while martensitic L80 lost more than half of its original ductility. This behavior is consistent with previously reported trends, where hydrogen primarily affects fracture strain rather than strength values [6, 13, 14]. The larger hydrogen uptake observed in L80 is explained by its tempered martensitic microstructure, which contains a high density of dislocations, carbides, and residual stresses that serve as trapping sites for hydrogen. Similar findings have been reported for other high-strength martensitic steels, where increased trapping capacity enhances susceptibility to hydrogen embrittlement [10, 12, 14].

Fractographic observations further support these conclusions, showing a transition from ductile dimple fracture in uncharged samples to quasi-cleavage fracture after hydrogen charging. While both steels exhibited this transition, the martensitic grade displayed more frequent secondary cracks in the necking area, consistent with hydrogen-assisted cracking reported in pipeline steels [15, 16]. These results underline that, despite its higher strength, the martensitic steel L80 is not immune to hydrogen embrittlement and in fact may show higher sensitivity than the lower-strength ferritic–pearlitic CSN 12022.

6 Conclusion

This study demonstrated that both ferritic–pearlitic CSN 12022 and martensitic L80 steels are significantly affected by hydrogen embrittlement.

Electrolytic hydrogen charging increased the absorbed hydrogen content by approximately fivefold in both materials, with L80 showing higher absolute uptake. Tensile tests confirmed that hydrogen had little effect on strength but caused severe loss of ductility, reducing elongation from 39 % to 13 % in CSN 12022 and from 25 % to 11 % in L80. Fractography revealed a clear transition from ductile to brittle fracture modes after hydrogen exposure. These findings confirm that microstructure plays a decisive role in hydrogen susceptibility: the higher strength martensitic steel retains load-bearing capacity but exhibits limited ductility under hydrogen, while the ferritic–pearlitic steel suffers an even greater relative reduction in plasticity. For engineering practice, these results highlight the necessity of accounting for hydrogen effects when selecting and applying steels in energy, gas transport, or hydrogen-related technologies.

Acknowledgement

Supported by the OPST Project Green Energy Technologies Centre of UJEP, Reg. No CZ.10.02.01/00/24_061/0000462 and Programme Johannes Amos Comenius Project BIODEGRADABLE: Platform for modern implantology - research on individualized biodegradable materials, Reg. No CZ.02.01.01/00/23_020/0008512. The grant of Specific university research – grant No A1_FCHT_2025_011 is also acknowledged.

References

[1] LV, B., ZHANG, F. C., LI, M., HOU, R. J., QIAN, L. H.,WANG, T. S. (2010). Effects of phosphorus and sulfur on the thermoplasticity of high manganese austenitic steel. In: *Materials Science and Engineering: A*, Vol. 527, No. 21, pp. 5648-5653.

[2] MACIEJEWSKI, J. (2015). The Effects of Sulfide Inclusions on Mechanical Properties and Failures of Steel Components. In: *Journal of Failure Analysis and Prevention*, Vol. 15, No. 2, pp. 169-178.

[3] ATKINS, T. (2018). The importance of toughness in manufacturing. In: *Journal of Materials Processing Technology*, Vol. 261, No. 280-294.

[4] PERKA, A. K., JOHN, M., KURUVERI, U. B.,MENEZES, P. L. (2022). Advanced High-Strength Steels for Automotive Applications: Arc and Laser Welding Process, Properties, and Challenges. In: *Metals*, Vol. 12, No. 6, pp. 1051.

[5] DIEGO BELATO, R., WIM DE, W., DIRK, V.,STIJN, H. (2013). Latest developments in mechanical properties and metallurgical features of high strength line pipe steels. In: *International Journal of Sustainable Construction and Design*, Vol. 4, No. 1, pp.

[6] SHIRYAEV, A. G., CHETVERIKOV, S. G., CHIKALOV, S. G., PYSHMINTSEV, I. Y.,KRYLOV, P. V. (2018). Production of Seamless Steel Pipe for Oil and Gas Extraction in Challenging Conditions. In: *Steel in Translation*, Vol. 48, No. 11, pp. 704-711.

[7] BĘBEN, D. (2021). The Influence of Temperature on Degradation of Oil and Gas Tubing Made of L80-1 Steel. In: *Energies*, Vol. 14, No. 20, pp. 6855.

[8] OKONKWO, P. C., BARHOUMI, E. M., BEN BELGACEM, I., MANSIR, I. B., ALIYU, M., EMORI, W., UZOMA, P. C., BEITELMAL, W. H., AKYÜZ, E., RADWAN, A. B.,SHAKOOR, R. A. (2023). A focused review of the hydrogen storage tank embrittlement mechanism process. In: *International Journal of Hydrogen Energy*, Vol. 48, No. 35, pp. 12935-12948.

[9] DRAJEWICZ, M., PRZYBYLO, A., JOPEK, J., GORAL, M., KOSCIELNIAK, B., OCHAL, K., KUBASZEK, T., GURAK, A., DYCHTON, K., WOZNIAK, M., KWASNIEWSKI, P., KAWECKI, A., GLUCHOWSKI, W.,LAGODA, M. (2022). The Diffusion Coatings for Industrial Tool Application. In: *Manufacturing Technology Journal*, Vol. 22, No. 5, pp. 530-541.

[10] NORFLEET, D. M.,BEAVERS, J. A., Stress-Corrosion Cracking of Carbon and Low-Alloy Steels (Yield Strengths Less Than 1241 MPa)[1], in Stress-Corrosion Cracking: Materials Performance and Evaluation, R. H. Jones, Editor. 2017, ASM International. p. 0.

[11] JIANG, S., ZHANG, S., LIN, J., ZHU, X., LI, S., SUN, Y., XIA, Y., LIU, W.,WANG, C. (2023). Study on the Microstructure and Mechanical Properties of Martensitic Wear-Resistant Steel. In: *Crystals*, Vol. 13, No. 8, pp. 1210.

[12] SOBOLA, D.,DALLAEV, R. (2024). Exploring Hydrogen Embrittlement: Mechanisms, Consequences, and Advances in Metal Science. In: *Energies*, Vol. 17, No. 12, pp. 2972.

[13] CAVALIERE, P., Hydrogen Embrittlement: The Case of High-Strength Steels, in Hydrogen Embrittlement in Metals and Alloys. 2025, Springer Nature Switzerland: Cham. p. 487-548.

[14] ROSENBERG, G.,SINAIOVA, I. (2016). Hydrogenation Conditions which Do Not Result in Formation of Cracks During Hydrogen Charging Process of Steels. In: *Manufacturing Technology Journal*, Vol. 16, No. 5, pp. 1129-1135.

[15] GIANNINI, L., RAZAVI, N., ALVARO, A.,PALTRINIERI, N. (2024). Embrittlement, degradation, and loss prevention of hydrogen pipelines. In: *MRS Bulletin*, Vol. 49, No. 5, pp. 464-477.

[16] FALAT, L., ČIRIPOVÁ, L., PUCHÝ, V., PETRIŠINEC, I.,DŽUNDA, R. (2025). Effect of Electrochemical Hydrogen Charging on the Notch Tensile Properties of Natural Gas Transportation Pipeline Steel with Electroless-Plated Coatings and Their Adhesiveness Characterization. In: *Metals*, Vol. 15, No. 9, pp. 1032.

[17] KORECEK, D., SOLFRONK, P.,SOBOTKA, J. (2023). Utilization of Metal Forming Process Mathematical Modelling to Predict the Spring-back of the Dual-phase Steel Stamping. In: *Manufacturing Technology Journal*, Vol. 23, No. 6, pp. 827-836.